

Cite this: DOI: 10.1039/xxxxxxxxxx

Friction controls even submerged granular flows[†]

Juha Koivisto,^{*a,b} Marko Korhonen,^a Mikko Alava,^a Carlos P. Ortiz,^b Douglas J. Durian^b and Antti Puisto^a

Received Date

Accepted Date

DOI: 10.1039/xxxxxxxxxx

www.rsc.org/journalname

We investigate the coupling between interstitial medium and granular particles by studying the hopper flow of dry and submerged system experimentally and numerically. In accordance with earlier studies, we find, that the dry hopper empties at a constant rate. However, in the submerged system we observe the surging of the flow rate. We model both systems using the discrete element method, which we couple with computational fluid dynamics in the case of a submerged hopper. We are able to match the simulations and the experiments with good accuracy by fitting the particle-particle contact friction for each system separately. Submerging the hopper changes the particle-particle contact friction from $\mu_{vacuum} = 0.15$ to $\mu_{sub} = 0.13$, while all the other simulation parameters remain the same.

1 Introduction

Understanding the coupling between solid particles and liquid is a challenging task due the complexity of grain-grain and grain-liquid interactions^{1,2}. Even in vacuum the assemblies of granular particles exhibit highly complex dynamics. Depending on the loading and density, it can appear in gaseous, fluid-like or solid-like phases³. Related to this, the rheological characteristics of granular matter falls into the category of yield stress fluids^{4,5}. However, their behavior is even more complex, as many of them show discontinuous shear thickening at intermediate shear⁶. Such an effect is attributed to the interparticle friction and/or the interlocking of the grains, depending on their shape^{7–9}.

The 3D hopper flow, shown in Fig. 1, is a well studied model case of grain flow^{10–12}, partly due to the fact that the geometry is simple allowing for easy implementation for the experimentalists, but also due to its importance in practical applications, from simple silos in farms to complex pharmaceutical factories. Even in a hopper flow, all three granular phases exist: the gas phase outside the hopper, the solid phase near the hopper boundaries, and the yielded (fluid) phase directly above the orifice enabling the flow.

Numerous studies have shown that in a dry hopper, the outflow of the granular particles follows the Beverloo equation^{13–15}, which states that the grain outward flux remains constant in time

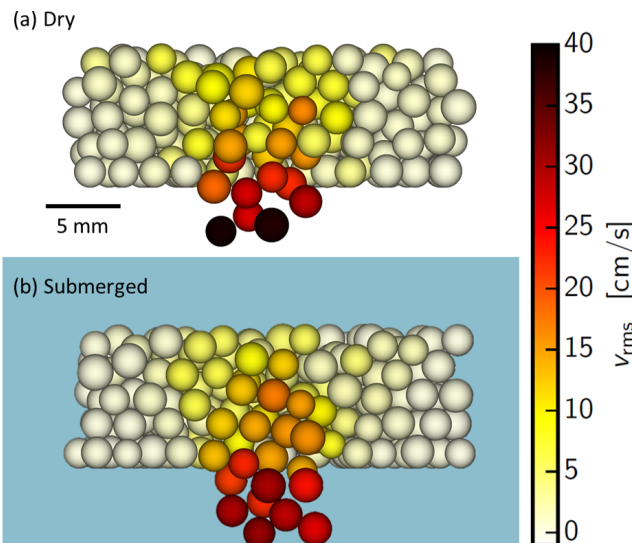


Fig. 1 Snapshot of the simulation close from the orifice shows the localized particle velocities. Here, the 3D cylinder is visualized at the center plane. In the vacuum system, the flux is fully driven by gravity pulling the particles out from the hopper. In the submerged case in addition to gravity the particle flux is driven by the fluid pushing the particles. Due to this, the particle volume fraction at the exit is higher in the submerged case (b) compared to vacuum (a) as is visually evident.

until the hopper empties. The Beverloo equation for a dry case

$$W_{dry} = C \rho \sqrt{g} (D - kd)^{(5/2)} \quad (1)$$

describes the mass flow rate as a function of the density ρ , gravity g as well as particle d and orifice D diameters. The term $D - kd$ illustrates the empty annulus where the particles partially reduce the size of the orifice through constant k . The exponent 5/2 can

^a Department of Applied Physics, Aalto University, Aalto 00067, Finland. Tel: +358 9 47001; E-mail: juha.koivisto@aalto.fi

^b Department of Physics and Astronomy, University of Pennsylvania, Philadelphia, Pennsylvania 19104-6396, USA.

[†] Electronic Supplementary Information (ESI) available:
https://www.youtube.com/playlist?list=PLlB0dcWeUNfvPvM6nAU1KsGv_4wbMKPw

be derived through the so called free fall theorem that essentially says that the flow rate is proportional to the particle velocity as if it would freely fall from granular bulk forming a semisphere above the orifice^{16–18}. The geometry then dictates the exponent 5/2. The Beverloo equation has the drawback that it only considers the dimensions of the grains and the orifice but not the properties of the interstitial medium, such as viscosity or drag.

Some studies have considered the role of air as an interstitial medium¹⁹. There are simulations and experiments that show non-trivial flow patterns of air due to particle motion, showing oscillations^{20,21} and flows resembling turbulence²². This movement of gas affects the flow of grains by creating pressure gradients and drag. These effects are in this case minor, since the drag caused by air is rather modest.

When the grains are embedded in a liquid, whose viscosity is orders of magnitude larger compared to that of air, the effect of interstitial medium is expectedly more pronounced²³. Recently the Beverloo equation was adapted and simplified to include the interstitial liquid¹¹

$$W_{go} = C \rho v_t d^2 (D/d - k)^2. \quad (2)$$

Here the acceleration due to gravity in fixed distance is replaced by terminal velocity v_t of a single particle in a liquid. Here, we mark the flow rate W with a subindex go to emphasize that this is the reference flow rate for infinitely high packings with passive fluid flow at the steady state²³. The empirical fit parameters are $C = 0.4$ and $k = 2.4$ ^{11,23}. In addition, as opposed to a Newtonian fluid running out of a bucket, where the flow rate decreases as the fluid runs out, in the submerged granular system the flow rate of grains is observed to increase in time, i.e. surges¹¹. In this submerged granular flow, the complexity of the problem rises from the fluid-particle interactions. As in the dry hopper scenario, the driving force of the system is the particle flow created by gravity. However, here the motion of the particles additionally creates fluid flow that disturbs the particle trajectories. This feedback loop between fluid and particles presumably increases the driving pressure of grains as they run out. A simple analytical model taking this into account is already shown in Reference²³.

The article is organized as follows: It starts by introducing the reader to our Methods, giving the details of both the experiments and the simulations. Then in the section Results we describe the main findings, showing that the features observed in experiments are captured by the simulations. Once the validity of the simulation is confirmed, the values of grain-grain friction is varied in the simulations. The article finishes with Conclusions, where we discuss the results, and give the readers a short overlook to future research.

2 Methods

Here, we study both the dry and submerged granular hopper flows. In the simulations, we assume that we can model the dry case without the interstitial fluid (no CFD), since air viscosity and density are negligible. In contrast, the submerged granular flow comprises two distinct phases (granular particles and liquid) that interact by various forces and have to be modeled concurrently.

The approach adopted here is to model the liquid phase on a continuum level and the granular phase as discrete particles. Specifically, the fluid phase is modeled by the Computational Fluid Dynamics (CFD) method²⁴, which utilizes the Finite Volume Method (FVM) for discretizing the Navier-Stokes in the problem domain. The Discrete Element Method (DEM)²⁵ is applied for the granular (particle) phase and each particle trajectory is integrated individually based on the interaction forces.

In the CFD framework, the modified Navier-Stokes equations (NSEs)²⁶, physically implying the conservation of mass and momentum, are discretized and solved to yield the relevant quantities, such as the local fluid velocity and pressure fields. For an incompressible fluid, these read¹

$$\begin{aligned} \frac{\partial \varepsilon_f}{\partial t} + \nabla \cdot (\varepsilon_f \mathbf{u}) &= 0, \\ \rho_f \varepsilon_f \left[\frac{\partial \mathbf{u}}{\partial t} + \nabla \cdot (\mathbf{u} \mathbf{u}) \right] &= \nabla \cdot \boldsymbol{\tau} - n \mathbf{f}_i + \rho_f \varepsilon_f \mathbf{g}, \end{aligned} \quad (3)$$

where ε_f is the fluid volume fraction, \mathbf{u} is the fluid velocity, ρ_f is the fluid density, $\boldsymbol{\tau}$ is the Cauchy stress tensor and \mathbf{g} is the gravity term. Additionally, these modified NSEs include the particle-fluid interaction term ($n \mathbf{f}_i$), that contains the sum of the appropriate interaction forces over a number of particle n , such as the (Di Felice) drag force²⁷, buoyancy, pressure gradient forces and the imposed shear stress². This term is also present in the DEM scheme, where it is included in the Newton's 2nd law which is formulated and solved for each particle. More specifically, the equations of motion in DEM are¹

$$\begin{aligned} m_i \frac{\partial \mathbf{v}}{\partial t} &= \mathbf{f}_i + \sum_{j=1}^{n_c} (\mathbf{f}_{c,ij} + \mathbf{f}_{d,ij}) + m_i \mathbf{g} \\ I_i \frac{\partial \omega_i}{\partial t} &= \sum_{j=1}^{n_c} (\mathbf{M}_{t,ij} + \mathbf{M}_{r,ij}), \end{aligned} \quad (4)$$

where m_i is the mass of particle i , \mathbf{v} is the velocity of the said particle, $\mathbf{f}_{c,ij}$ and $\mathbf{f}_{d,ij}$ describe the elastic deformation and viscous energy dissipation of the particle while in contact with particle j . Further, I_i is the moment of inertia of the particle while $\mathbf{M}_{t,ij}$ and $\mathbf{M}_{r,ij}$ describe the torque generated by tangential forces in a collision and rolling friction, respectively. Here, we have set the rolling friction to zero.

The presented coupling scheme has the inherent advantage of providing an accurate description of both the fluid and the particle phase at a reasonable computational expense². Furthermore, the CFD-DEM coupling is realized in a readily implemented software called CFDEM project which combines the OpenFOAM CFD-library with a DEM solver (LIGGGHTS²⁸), providing the user extensive control over the simulation particulars and more importantly, the NSEs and fluid-particle interaction models¹. The implementation also grants efficient CPU parallel execution via the Message Passing Interface (MPI).

The material parameters used in the numerical method are obtained, where possible, from the experiments or utilizing textbook values. In the experiments, there are three types of grains, while in the simulations only the largest one is used. The grains are

technical quality soda lime silica glass beads with $d = 0.2 \pm 0.01$ cm (A-205), $d = 0.1 \pm 0.01$ (A-100) and $d = 0.05 \pm 0.005$ (P-230) in diameter from Potters Industries. Their density is $\rho = 2.54 \pm 0.01$ g/cm³ measured using the Archimedes method by sinking the beads in liquid and measuring the weight of the grains and fluid volume displacement. These values of the grain properties were set in the simulations to match the experimental values. The simulations additionally require knowledge of the elastic (Young's and shear) moduli, and the friction and restitution coefficients. The typical values for Young's and shear moduli of glass beads tabulated in textbooks are $E = 72$ GPa and $G = 30$ GPa, respectively. These give the Poisson's ratio of $\nu = E/(2G) - 1 = 0.2$. It has been shown that a lower value of Young's modulus can be used without affecting the results²⁹ and this is also what we have observed while benchmarking our algorithm. The parameters used in the simulations are summarized in Tab. 1.

The friction and restitution coefficients, describing the dissipation of the grain-grain contacts and collisions, are the remaining parameters required to perform DEM simulations. Measurement of either of these for glass beads is impractical as it requires to estimate the dissipated energy in a dense granular flow. A textbook value for sliding of wet glass surfaces is around $\mu = 0.1$, which can be taken as a starting point for the simulations. A sensible value for the restitution coefficient of hard-sphere-like glass beads is $\alpha = 0.9$. For instance, in similar dry simulations involving softer grains, the restitution coefficient of $\alpha = 0.8$ has been used³⁰.

In the experimental setup, the liquid phase consists of filtered tap water at $T = 22$ °C temperature with the well known textbook values for viscosity $\eta = 1.0$ mPa·s and density $\rho_f = 1.00$ g/cm³. Accordingly, these values were used in the simulations, with the further assumption of laminar flow conditions. Laminar flow can be safely assumed owing to the fact that the flow rates remain rather modest being purely driven by the release of the grains' potential energy. In practice the hopper is submerged in a large fish tank. There are no water – air interfaces. The experiment is

Table 1 The values for the particle and fluid properties applied in the simulations and experiments. The more detailed technical information on the simulations is provided as Supplementary Data 1. The values marked with star are textbook values.

		simulation	experiment
Granular particles			
Density of glass	ρ [g/cm ³]	2.5	2.54
Young's Modulus	E [GPa]	0.025	72*
Shear Modulus	G [GPa]	–	30*
Poisson's ratio	ν	0.2	0.2 *
Restitution coefficient	α	0.9	–
Timestep (DEM)	dt [μ s]	5.0	–
Fluid			
Density of water	ρ_f [g/cm ³]	1.0	1.0*
Viscosity	η [mPa · s]	1.0	1.0*
Timestep (CFD)	dt [μ s]	50.0	–
Coupling interval	$d\tau$ [μ s]	500.0	–

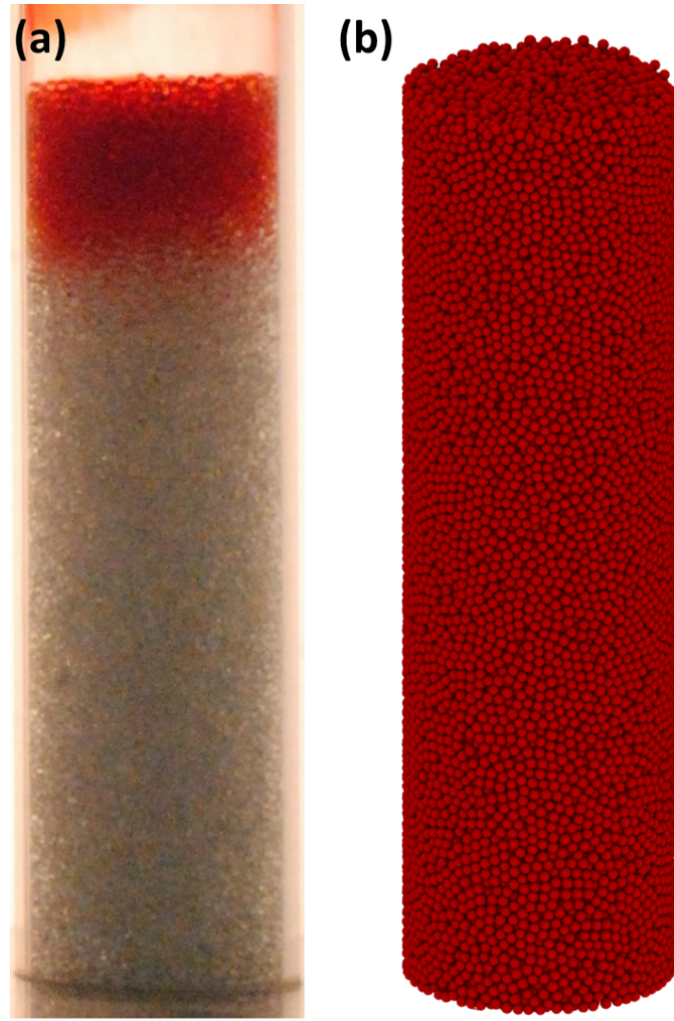


Fig. 2 Experimental (a) and numerical (b) geometries are the same; The orifice diameter is $D = 1.0$ cm, particle diameter $d = 0.2$ cm and hopper diameter $D_h = 5.0$ cm. The red dye injected on top of the grains in the experiments (a) is visualizing the fluid flow. The grains are transparent glass but appear albescent.

totally under water. The scale is above the water level, measuring the weight of the remaining beads in the hopper. The hopper is a flat bottomed cylindrical tube made of transparent polycarbonate with $D_h = 5.0$ cm diameter. The orifice is a circular hole ($D = 1.0$ cm) with 1 mm vertical walls that expand in 45-degree bevel cut at the center of the aluminum bottom. The experimental setup is described in detail in Refs.^{23,31} and their supplemental material.

Fig. 2 displays both the experimental 3D hopper (a) as well as its simulation counterpart (b). The initial state of the experimental hopper contains 50 % more beads than shown in Fig. 2(a). The red dye at the top was injected on top of the granular pile before the experiment and it propagates through the hopper faster than the grains can exit the system. (See the supplementary videos 1 and 2 which illustrate this process.)

The geometry is the same in the simulations and experiments, with very few exceptions. The initial filling height is smaller in the simulations, the hopper walls possess no thickness and have

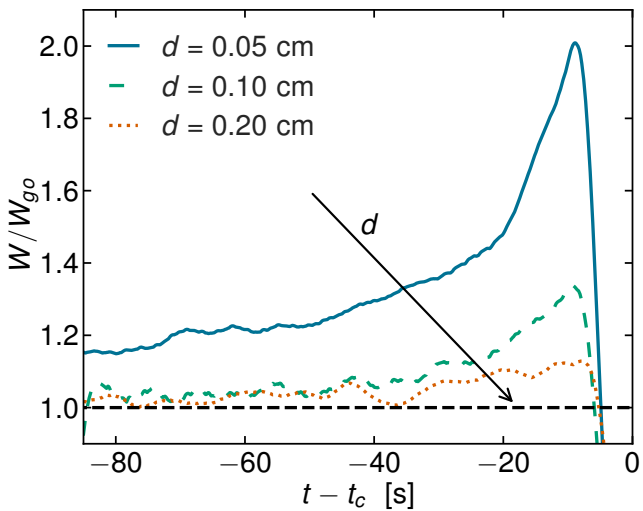


Fig. 3 The relative mass flow rate of hopper for three different particle sizes. The flow rate W is normed with the flow rate W_{go} depicted with dashed line that is the asymptotic reference flow rate for infinitely high packings. We find that the surge, the acceleration at the end decreases as particle size increases.

the same friction coefficient as the grains. The CFD simulation domain is divided into 1.5 million cells. The grid size gradually decreases near the hopper boundaries to ensure the quality of the solution in those areas. The meshing is realized applying the snappyHexMesh-tool embedded in the OpenFOAM software³².

In the simulations, the hopper flow is generated by first filling the hopper with the granular medium by pouring randomly the particles above the hopper top while the orifice remains closed. Then, once a sufficient filling height h is obtained, the granular packing is allowed to relax without the fluid for 0.5 seconds. At this point, the selection between the vacuum and submerged cases is made. In the vacuum case the orifice is opened, and the simulation is continued. In the submerged case, the coupled CFD-DEM simulation is initiated and the orifice is opened.

3 Results

Motivated by the large computational cost of the prescribed numerical simulations, we revisit our earlier experimental findings with a new perspective. The goal is to find a good compromise between having a long enough experiment with good surge per noise ratio (improves by reducing the particle size) and the computational burden (decreases with increasing particle size). The total particle number that can be handled with reasonable computational cost can be reached using the average grain diameter of $d = 0.2$ cm. Our main concern is the impact of the particle size on the surge. Hence, we start by comparing the earlier studied systems having $d = 0.05$ cm and $d = 0.1$ cm²³ to the new system with $d = 0.2$ cm. For this purpose, we observe the flow rate and compute selected dimensionless numbers characterizing the systems

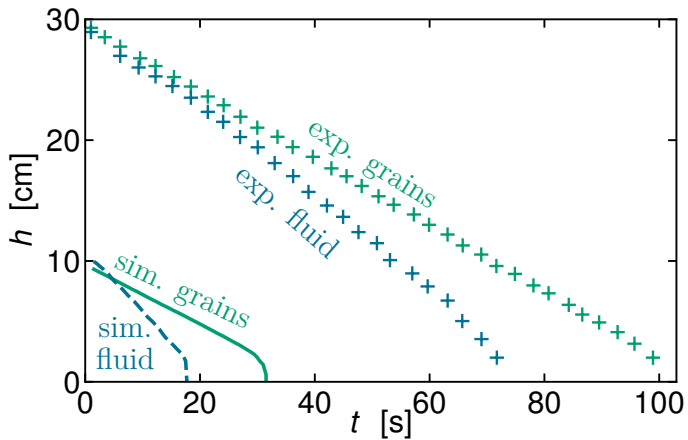


Fig. 4 The Fluid-is-Faster effect is illustrated by plotting the trajectories of tracer particles. The green symbols represent the height of the granular column where the tracer particle is the highest particle at the side of the hopper. The blue symbols depict the lower edge of the dye. In the simulations, the blue dashed curve represents the vertical position of a single point-like virtual fluid tracer obtained by post processing the continuum fluid field. The green curve is the vertical position of one of the simulated grains. The figure shows that the fluid has a greater superficial velocity in both cases. The experiment and simulation are not directly comparable as the experimental values are averages while the simulation values are point-like measurements.

Fig. 3 shows the relative flow rate against time $t - t_c$, where the t_c is the time when the flow stops. The flow rate W is obtained by differentiating the mass time series of the scale by fitting a 2nd degree polynomial in a 2 second Gaussian window similarly to Ref.²³. As we are interested on the surge and dynamic effects we scale the data by the reference flow rate obtained from the modified Beverloo equation (2). This operation allows us to compare the surge between the systems having different particle sizes.

The surge, the increase of flow rate W with respect to the asymptotic value W_{go} decreases with increasing particle size as highlighted by the black arrow in Fig. 3. Also, the lifetime of the surge decreases when particle size increases which makes the comparison to simulations easier for larger particles than the small ones. The largest increase $W_{surge} = \max(W) - W_{go}$ is with $d = 0.05$ cm particles and the smallest is with $d = 0.2$ cm particles. This agrees with earlier findings as the surge term containing the fluid-grain coupling has d dependence as $W_{surge} \propto (D - kd)^2$ (after expanding α from the supplementary material in Ref.²³). The surge W_{surge} thus decreases when approaching the clogging region from below by increasing the particle size d . There is no flow, nor surge above the clogging region. We conclude that the large particles in our case approach to a limit where the granular aspect of the system starts to dominate. The inertia of the grains is too high for the fluid that there would be a large surge.

Fig. 4 points out, that the superficial fluid velocity is faster than the grain velocity²³. The fluid is faster and the inertia of the particles decreases the flow rate while the viscous component increases the flow. This counterintuitive result is consistent with the earlier results²³ and illustrated in supplementary video 1 with a layer of dye that propagates faster than the grains can exit. With

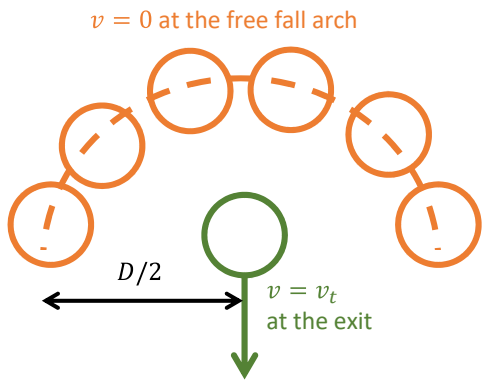


Fig. 5 Schematic illustration of the particles at the orifice of size D accelerating from rest (orange) to terminal velocity (green) due to gravity and thus creating shear.

small particles the fluid flow dominates the process and particles reflect to this. The large particles have more momenta and inertia. The fluid flow cannot affect the particle motion. Then, the granular characteristics of the large particles dominate.

To obtain a more rigorous treatment we calculate dimensionless numbers that describe the flow. Table 2 describes the dimensionless numbers of the system. The Reynolds number $Re = \rho_f v_t d / \eta$ describes the ratio of inertial forces with respect to viscous forces. It increases dramatically as the particle diameter increases ($Re \approx d^2$) indicating the increase of granular behavior at the expense of fluid flow, provided the grain properties (grain-grain friction, and grain size distribution) remain the same. At the same time, the drag coefficient decreases³³, again, indicating the diminishing effect of fluid. Note that here we discuss only the laminar flow case. Finally we calculate the inertial number that is the ratio of confining pressure and shear rate $I = \eta \dot{\gamma} / P$ ^{34,35}. The inertial number I can be approximated by defining the shear rate $\dot{\gamma} = v_t / (D/2)$ as velocity difference at the orifice and an approximation of driving pressure $P = 1/2 \rho_e v_t^2$ as

$$I = \eta \frac{\dot{\gamma}}{P} = \eta \frac{D}{\rho_e v_t}, \quad (5)$$

where the effective density ρ_e is the buoyancy corrected density. The particle geometry at the orifice is illustrated in Fig. 5. For small particles the inertial number is large, at the region where the dynamic effects already play a role. For large particles the inertial number decreases and the dynamic friction coefficient saturates (close) to static value³⁶. This is seen as a lack of terminal surge as a constant dynamic friction coefficient $\mu(I)$ indicates constant flow rate. Also, recently³⁷ it has been numerically found that the ratio of frictional and viscous dissipation changes in submerged particle systems. Here, we are approaching the frictional regime from viscous regime by increasing the particle size leading to vanishing surge.

The experimental study extends the research to larger particles in order to reduce the particle number to a sufficient level to enable numerical simulations. Not only the flow rate, but also the surge at the end of the experiment, depends on the particle diameter. As we have a grasp of the experimental aspects of the

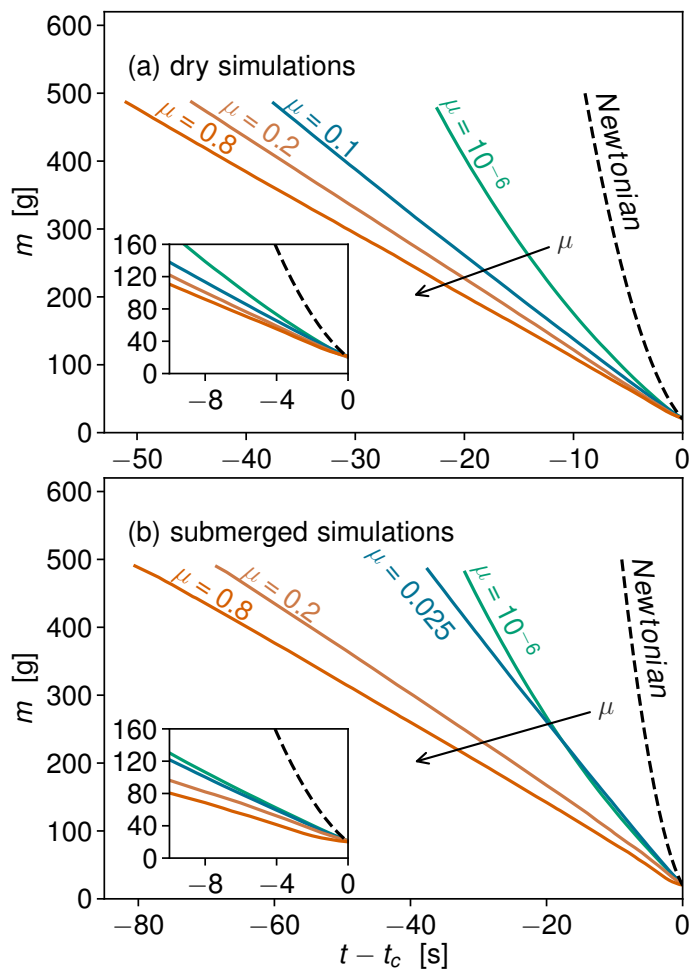


Fig. 6 (a) The mass of grains inside the hopper as a function of time for various values of friction coefficient μ for the dry system. For nearly frictionless case (green, $\mu = 10^{-6}$) the flow rate (slope) is high and decreases as the grains flow out. This corresponds to what happens with a Newtonian fluid (dashed curve). For high friction case (red, $\mu = 0.8$) the behavior is linear with constant flow rate and corresponds to the standard Beverloo equation. (b) The mass of particles inside a hopper as a function of time for the submerged system. For low friction coefficients the flow rate (slope) is decreasing similarly to the dry case. The insets show the magnification of the datasets near the end.

particle size dependence of the surge, it is possible to pick the largest particle size $d = 0.2$ cm as a representative case.

In the simulations the low friction granular (cyan) and the Newtonian fluid (dashed black) cases in Fig. 6(a) are non-linear and therefore not described by the Beverloo equation (2). The inset in Fig. 6(a) shows the magnification of the data near the end of the experiment. This is to point out that there seems to be no

Table 2 Dimensionless numbers characterizing the system are the Reynold's number (Re) and the inertial number I .

d [cm]	Re	C_d	I
0.05	37	1.76	34.0×10^{-4}
0.10	151	0.86	17.0×10^{-4}
0.20	530	0.56	9.8×10^{-4}

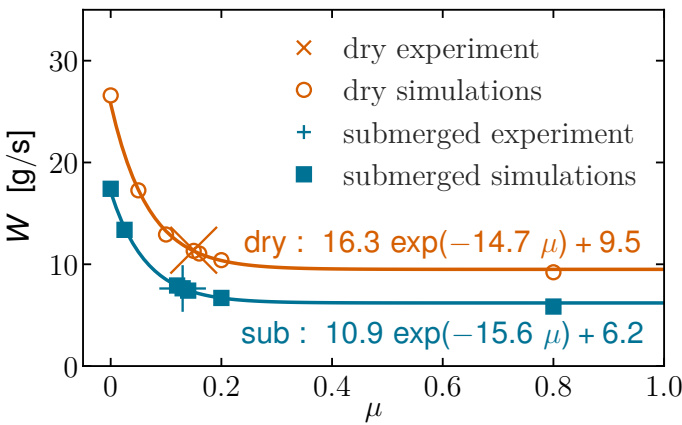


Fig. 7 Flow rate at the beginning of the experiment versus friction coefficient for dry (red open circles) and submerged (blue filled squares) extracted from previous figures. The fit and functional form is purely empirical and used in finding the matching friction coefficient. The behavior appears to be exponential in this narrow region, highlighting how sensitive the flow rate is to the value of contact friction. Here we anticipate the experimental results by plotting the mass flow rate in dry experiments (red x) at $W_{dry} = 11.4$ g/s corresponding friction coefficient $\mu_{dry} = 0.15$ in the simulations. Similarly, the mass flow rate in submerged experiments (blue $+$) is $W_{sub} = 7.6$ g/s corresponding to friction coefficient $\mu_{sub} = 0.13$ in simulations.

acceleration in the flow rate.

Next, we repeat the simulation with parameters identical to the dry case with the exception that the grain-liquid coupling is enabled. Fig. 6(b) shows the mass in the hopper over $t - t_c$ as displayed earlier for the dry case in Fig. 6(a). The initial conditions, material parameters (except the friction coefficients), geometry, number of particles and even the initial particle locations are the same in each case. The largest difference is that the flow rates are significantly lower in the submerged cases. For instance, the simulation with the friction coefficient $\mu = 0.8$ takes 52 seconds to empty 500 grams of grains in the dry case, while in the submerged case it takes 90 seconds.

Additionally, there is an acceleration of the flow rate at the end of the simulation (Fig. 6 insets). This is seen as separation of datasets and a slight downwards tilt in the data for the larger friction coefficients. Again, following the dry case, the low friction cases behave like Newtonian fluids without the acceleration. The contact friction of bulk granular materials is typically above $\mu = 0.1$. For these values, we find a surge like feature in the submerged simulation, lacking from the dry case. As the only difference between the dry and submerged simulation is the inclusion of fluid, we conclude that the surge is due to the coupling between the liquid and grains. In Fig. 7, we plot the simulated flow rate W with multiple values of the friction coefficient μ , creating an empirical relation between the initial flow rate W and the friction coefficient μ . Based on this empirical relation we deduce the friction coefficient by matching the flow rates in the experiments at $m = 300 \dots 400$ g. The red open circles correspond to the dry simulations and the filled blue squares to the submerged simulations. The friction coefficients that reproduce the experiment are almost equal as $\mu_{dry} = 0.15$ and $\mu_{sub} = 0.13$ in the dry and submerged cases, respectively. The similarity in dry and submerged

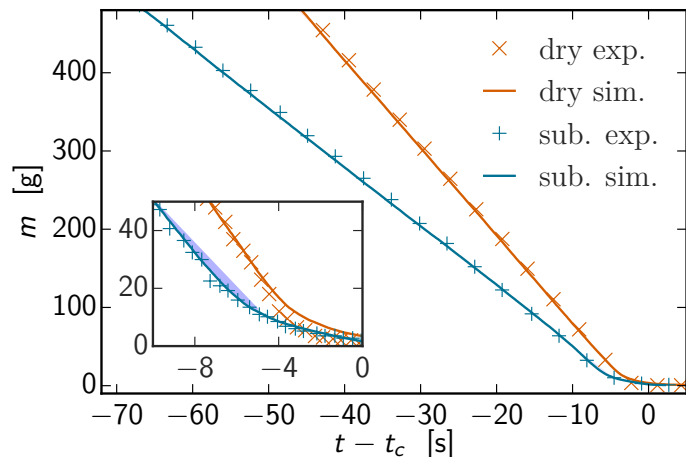


Fig. 8 The raw data from the experiments and simulations show the difference between dry (red) and submerged (blue) case. The linear fit depicted with solid line to the simulation data above $m = 200$ g matches the dry case perfectly until the grains run out. In submerged case the data takes a nose dive, surges, before the grains run out. Inset: the blue area indicates a surge, the difference between linear Beverloo behavior and measured data.

friction coefficient is also reported by Dijksman *et al.* with acrylic beads in a rheometer³⁸. Note that here we refer to grain-grain friction whereas Dijksman *et al.* refers to the minimum friction coefficient μ_o at the quasi-static limit when inertial effects vanish $I \rightarrow 0$. The relation $\mu_o(\mu)$ is a non-trivial monotonic function that (to our knowledge) is only explored numerically^{37,39,40}.

Fig. 8 displays the mass of grains remaining in the hopper from both the experiments and the simulations with the friction coefficient set to the obtained values of $\mu_{dry} = 0.15$ in the dry case and $\mu_{sub} = 0.13$ in the submerged case. The submerged experiment is depicted in blue and the dry case in red color. The datasets are the result of a single run. The simulated and the experimental data are overlapping within the measurement accuracy. This lends credence to the computational approach applied in the work and specifically suggests that the coupled CFD-DEM model captures the quintessential features of the two-phase (submerged) hopper flow.

The nonlinear surge effect is highlighted in the insert with a blue area that is the difference between a linear fit and the experimental data before the flow rate slows down. The blue area is drawn to both cases, dry and submerged but is visible only in the submerged case. This indicates that the constant flow rate predicted by the Beverloo law applies to the dry case but does not apply to the submerged case.

Fig. 9 displays the Gaussian weighted derivative over two second time window of the data depicted in Fig. 8. In both dry cases, the experiment and the simulation, the hopper empties at a constant flow rate. At the end when the grains run out and the flow rate decreases without a terminal surge. In contrast, the presence of the interstitial fluid reduces the overall granular flow rate and imposes an acceleration towards the end. Recently, such terminal surge has been confirmed in the dry case for smaller particles in experiments²³ and appears to be visible also in simulations^{30,41}.

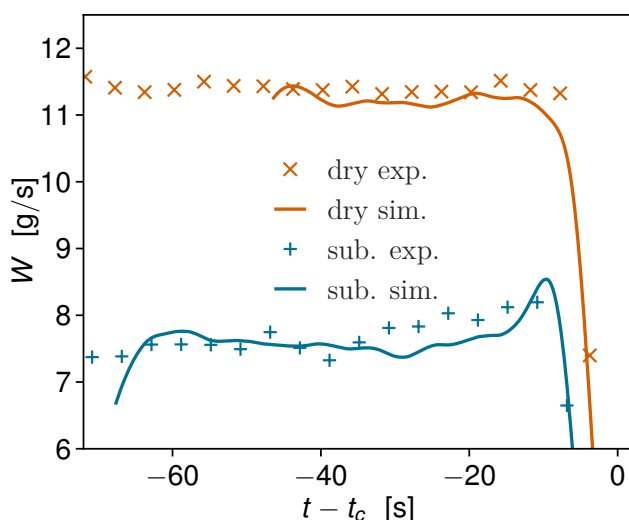


Fig. 9 The derivative of hopper mass over time shows the surge in submerged case for both experiments (blue +) and simulations (solid curve). The surge is not seen in the dry experiments (red x) and simulations (solid red). However, the final moments of the dry experiment might contain a tiny surge that is too fast for the current experimental procedure and analysis.

Based on our theoretical discussion on the terminal velocity, and on the dependence of the surge on particle size, we propose that the 2 mm particles are too heavy to be affected by interstitial air. Therefore, the surge does not appear in the dry experiments resulting in good agreement to our vacuum simulations. Since the viscosity and density of water are several orders of magnitude larger, the submerged flow exhibits a surge. We conclude that the viscosity of the interstitial medium has to be large enough compared to the particle inertia for the surge to appear.

Flow sensitivity to friction coefficient gives the possibility to interpret the hopper flow in the context of non-linear effective rheology. Fig. 10 shows a schematic illustration of three systems with (discontinuous) shear thickening⁴², a characteristic of frictional granular systems. For the same load, caused by the high particle column, the frictionless case, a Newtonian fluid, has the smallest slope and thus lowest effective viscosity. Friction increases the slope and introduces a sudden increase of viscosity, that can be many orders of magnitude. When the mass $m(t)$ of the particle column decreases in time, the effective viscosity of the system decreases as well, causing an increase in the flow rate. This is seen as the terminal surge.

4 Conclusions

We performed experiments and simulations on dry and submerged hopper flows of granular particles of approximately millimeter radius. Experimentally we confirm the previously known results, that in a system with dry frictional particles the flow rate remains constant until the height of the granular column is less than the width of the hopper⁴⁴. In the submerged system we find

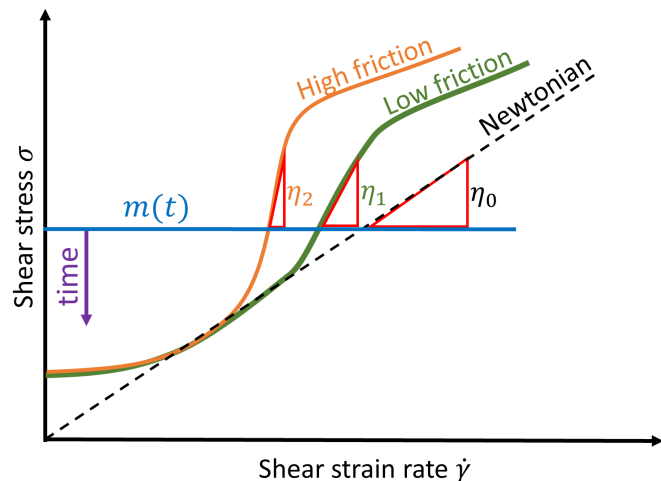


Fig. 10 A schematic illustration of three materials with discontinuous shear thickening. The increasing contact friction of the particles leads to decreasing flow rate. At continuum, this can be interpreted as increasing effective viscosity η_i that increases with particle friction for high shear stresses.

that the flow accelerates throughout the whole hopper emptying process in agreement with earlier work²³.

We modeled both, the dry and submerged systems using a method coupling CFD and DEM. In the method, the particle trajectories and interactions are computed explicitly in the DEM-implementation, whereas the fluid flow is modeled on a continuum level by the CFD approach. This makes it fundamentally different from the inertial $\mu(I_v)$ -model where the granular media and the interstitial fluid are treated as a single continuum⁴⁵. In a **dry** hopper our model finds two different behaviors, depending on the inter-particle friction: 1) Hopper filled with frictionless particles empties with a decreasing flow rate, much like a bucket filled with a Newtonian fluid, in agreement to earlier numerical work⁴³. 2) Hopper filled with frictional particles empties at a constant rate conforming to the well known hour glass or Beverloo behavior. Of these, the latter can be observed in the experiments here, and before⁴⁴.

In the **submerged** case, the model again exhibits two separate dynamics depending on the inter-particle friction: 1) Frictionless particles exit the hopper at a decreasing rate, conforming to Newtonian fluid flow. 2) In the frictional case the hopper empties at an increasing rate followed by a terminal surge, precisely following the experimental observation of a surging flow as observed in the present work, and as found before for smaller particles²³. This data further reinforces the granular pumping scenario suggested earlier²³.

Knowing both the dry and submerged cases were sensitive to the grain-grain friction allowed us to use it to fit the simulated flow rates against the corresponding experiments quantitatively. Subsequently, we observed that the best fit friction parameter is almost the same in both the cases. This was a surprising result, since one would expect the grain-grain friction to be significantly lower between the grains. However, as we do not explicitly ac-

count for the grain-grain hydrodynamic interactions, we expect the friction coefficient partly compensates for that.

Here we have presented the first step to compare simulations and experiments of a submerged hopper flow with a good agreement. The one-to-one match with experiments and simulation is currently pushing the limits of both methods. Using smaller than $d = 0.2$ cm particles increases the experimental accuracy via lowering the flow rate. However, using smaller particles in the simulations renders them impractical by making the problem too large for the present computational resources. Both of these problems, the experimental and numerical may be solvable in the near future by advanced computational methods such as coarse graining of particles in the bulk^{46,47} and experimental measurement techniques such as identifying and counting individual particles. Future studies could involve the effect of wall and bottom friction, dilation of grains at the orifice, clogging, self-generated pumping of fluid, terminal and exit velocities of particles, and the behavior of W_{go} as a function of particle size. For W_{go} there should be a transition from colloidal no-flow behavior to surging flow and back to no-flow at clogging, which unfortunately fell outside the scope of this paper.

5 Conflicts of interest

There are no conflicts to declare.

6 Acknowledgement

This work was supported by the Academy of Finland through the COMP Centre of Excellence and the project number 278367. The simulations were performed using the computer resources within the Aalto University School of Science, Science-IT project. JK acknowledges the support from Finnish Cultural Foundation and Wihuri foundation through Foundations' Post Doc Pool project. DJD acknowledges the support from NFS through grant DMR-1305199.

References

- 1 Z. Zhou, S. Kuang, K. Chu and A. Yu, *J. Fluid Mech.*, 2010, **661**, 482–510.
- 2 H. Zhu, Z. Zhou, R. Yang and A. Yu, *Chem. Eng. Sci.*, 2007, **62**, 3378–3396.
- 3 P. Eshuis, K. van der Weele, D. van der Meer, R. Bos and D. Lohse, *Phys. Fluids*, 2007, **19**, 123301.
- 4 T. Divoux, M. A. Fardin, S. Manneville and S. Lerouge, *Annu. Rev. Fluid Mech.*, 2015, **48**, 81.
- 5 D. H. Johnson, F. Vahedifard, B. Jelinek and J. F. Peters, *J. Rheol.*, 2017, **61**, 265–277.
- 6 R. Seto, R. Mari, J. F. Morris and M. M. Denn, *Phys. Rev. Lett.*, 2013, **111**, 218301.
- 7 W. Losert, J.-C. Géminard, S. Nasuno and J. P. Gollub, *Phys. Rev. E*, 2000, **61**, 4060–4068.
- 8 A. G. Athanassiadis, M. Z. Miskin, P. Kaplan, N. Rodenberg, S. H. Lee, J. Merritt, E. Brown, J. Amend, H. Lipson and H. M. Jaeger, *Soft Matter*, 2014, **10**, 48–59.
- 9 H. M. Jaeger, *Soft Matter*, 2014, **11**, 12–27.
- 10 C. C. Thomas and D. J. Durian, *Phys. Rev. E*, 2016, **94**, 022901.
- 11 T. J. Wilson, C. R. Pfeifer, N. Mesyngier and D. J. Durian, *Papers in Physics*, 2014, **6**, 060009.
- 12 C. C. Thomas and D. J. Durian, *Phys. Rev. Lett.*, 2015, **114**, 178001.
- 13 W. Beverloo, H. Leniger and J. V. de Velde, *Chem. Eng. Sci.*, 1961, **15**, 260.
- 14 M. A. Madrid, J. R. Darias and L. A. Pugnaloni, *EPJ Web Conf.*, 2017, **140**, 03041.
- 15 A. Ashour, S. Wegner, T. Trittel, T. Borzsonyi and R. Stannarius, *Soft Matter*, 2017, **13**, 402–414.
- 16 Y. Tian, P. Lin, S. Zhang, C. L. Wang, J. F. Wan and L. Yang, *Adv. Powder Technol.*, 2015, **26**, 1191–1199.
- 17 A. Janda, I. Zuriguel and D. Maza, *Phys. Rev. Lett.*, 2012, **108**, 248001.
- 18 C. Mankoc, A. Janda, R. Arévalo, J. M. Pastor, I. Zuriguel, A. Garcimartín and D. Maza, *Granul. Matter*, 2007, **9**, 407–414.
- 19 S. Yuu and T. Umekage, *Materials*, 2011, **4**, 1440–1468.
- 20 X.-l. Wu, K. J. Maloy, A. Hansen, M. Ammi and D. Bideau, *Phys. Rev. Lett.*, 1993, **71**, 1363–1366.
- 21 Y. Bertho, F. Giorgiutti-Dauphiné, T. Raafat, E. J. Hinch, H. J. Herrmann and J. P. Hulin, *J. Fluid Mech.*, 2002, **459**, 317–345.
- 22 J. E. Hilton and P. W. Cleary, *Phys. Rev. E*, 2011, **84**, 011307.
- 23 J. Koivisto and D. J. Durian, *Nat. Commun.*, 2017, **8**, 15551.
- 24 J. H. Ferziger and M. Peric, *Computational methods for fluid dynamics*, Springer, 2012.
- 25 P. A. Cundall and O. D. Strack, *Geotechnique*, 1979, **29**, 47–65.
- 26 T. B. Anderson and R. Jackson, *Ind. Eng. Chem. Fundamen.*, 1967, **6**, 527–539.
- 27 R. Di Felice, *Int. J. Multiphas. Flow*, 1994, **20**, 153–159.
- 28 C. Kloss, C. Goniva, A. Hager, S. Amberger and S. Pirker, *Prog. Comput. Fluid Dy.*, 2012, **12**, 140–152.
- 29 S. Lommen, D. Schott and G. Lodewijks, *Particuology*, 2014, **12**, 107–112.
- 30 S. R. Schwartz, D. C. Richardson and P. Michel, *Granul. Matter*, 2012, **14**, 363–380.
- 31 J. Koivisto and D. J. Durian, *Phys. Rev. E*, 2017, **95**, 032904.
- 32 *OpenFoam: The OpenSource CFD Toolbox*, OpenFoam Foundation, 2014.
- 33 F. A. Morrison, *Data Correlation for Drag Coefficient for Sphere*, www.chem.mtu.edu/~fmorrison/DataCorrelationForSphereDrag2016.pdf (accessed April 2017).
- 34 M. Houssais, C. P. Ortiz, D. J. Durian and D. J. Jerolmack, *Nat. Commun.*, 2015, **6**, 6527.
- 35 K. Kamrin and D. L. Henann, *Soft Matter*, 2015, **11**, 179–185.
- 36 A. Singh, V. Magnanimo, K. Saitoh and S. Luding, *New J. Phys.*, 2015, **17**, 043028.
- 37 M. Trulsson, E. DeGiuli and M. Wyart, *Phys. Rev. E*, 2017, **95**, 012605.

- 38 J. A. Dijksman, E. Wandersman, S. Slotterback, C. R. Berardi, W. D. Updegraff, M. van Hecke and W. Losert, *Phys. Rev. E*, 2010, **82**, 060301.
- 39 A. Lemaître, J. N. Roux and F. Chevoir, *Rheol. Acta*, 2009, **48**, 925–942.
- 40 F. da Cruz, S. Emam, M. Prochnow, J. N. Roux and F. Chevoir, *Phys. Rev. E*, 2005, **72**, 021309.
- 41 S. Dunatunga and K. Kamrin, *J. Fluid Mech.*, 2015, **779**, 483–513.
- 42 I. R. Peters, S. Majumdar and H. M. Jaeger, *Nature*, 2016, **532**, 214–217.
- 43 P. A. Langston, U. Tüzin and D. M. Heyes, *Chem. Eng. Sci.*, 1994, **49**, 1259–1275.
- 44 R. Nedderman, U. Tüzin, S. Savage and G. Houlsby, *Chem. Eng. Sci.*, 1982, **37**, 1597–1609.
- 45 F. Boyer, É. Guazzelli and O. Pouliquen, *Phys. Rev. Lett.*, 2011, **107**, 188301.
- 46 C. Bierwisch, T. Kraft, H. Riedel and M. Moseler, *J. Mechan. Phys. Solids*, 2009, **57**, 10–31.
- 47 D. Queteschner, T. Lichtenegger, S. Schneiderbauer and S. Pirker, *Progress in Applied CFD*, 2017, 773–778.